POLITECNICO DI TORINO
Repository ISTITUZIONALE

Robocasting of multicomponent sol-gel–derived silicate bioactive glass scaffolds for bone tissue engineering

Original
Robocasting of multicomponent sol-gel–derived silicate bioactive glass scaffolds for bone tissue engineering / Fiume, E., Massera, J., D'Ambrosio, D., Verne', E., Baino, F.. - In: CERAMICS INTERNATIONAL. - ISSN 0272-8842. - ELETTRONICO. - 48:23(2022), pp. 35209-35216. [10.1016/j.ceramint.2022.08.121]

Availability:
This version is available at: 11583/2977779 since: 2023-04-05T15:10:40Z

Publisher:
Elsevier

Published
DOI:10.1016/j.ceramint.2022.08.121

Terms of use:

This article is made available under terms and conditions as specified in the corresponding bibliographic description in the repository

Publisher copyright
Elsevier postprint/Author's Accepted Manuscript

© 2022. This manuscript version is made available under the CC-BY-NC-ND 4.0 license
http://creativecommons.org/licenses/by-nc-nd/4.0/.The final authenticated version is available online at:
http://dx.doi.org/10.1016/j.ceramint.2022.08.121

(Article begins on next page)

26 November 2026

Robocasting of multicomponent sol-gel–derived silicate bioactive glass scaffolds for bone tissue engineering

Elisa Fiume[1], Jonathan Massera[2], Daniele D'Ambrosio[1], Enrica Verné[1], Francesco Baino[1,*]

[1] Department of Applied Science and Technology (DISAT), Politecnico di Torino, 10129 Turin, Italy

[2] Faculty of Medicine and Health Technology, Tampere University, 33720 Tampere, Finland

*Corresponding author: F. Baino

E-mail: francesco.baino@polito.it

Tel. +39 011 090 4668

Abstract

Robocasting is universally recognized as an affordable and reproducible manufacturing strategy to process glass and glass-ceramic materials in the form of highly ordered porous scaffolds for bone tissue engineering (BTE) applications. Nevertheless, while being widely applied to melt-derived bioactive glasses, this technique was seldom implemented with sol-gel materials due to the intrinsic difficulties in producing suitable inks for extrusion and thus, good printing outcomes. The present experimental work describes a new and relatively easy method to manufacture multicomponent sol-gel bioactive silicate scaffolds (oxide system: 47.5SiO_2-20CaO-10MgO-10Na_2O-10 K_2O-

2.5P_2O_5, mol.%) using dried gels as basic material within the ink composition, which allows by-passing intermediate heat treatments that are usually detrimental to the bioactive potential of the material in physiological environment. The scaffolds, exhibiting a total porosity of 81 vol.%, were characterized in terms of morphological-compositional features and bioactivity in simulated body fluid (SBF), paying special attention to ion release and surface modifications occurring upon soaking (apatite-forming ability). The compressive strength of the scaffolds (around 5 MPa) was comparable to that of human cancellous bone. Collectively, the results supported the possibility of using robocast sol-gel–derived scaffolds in BTE approaches. Furthermore, a comparison with robocast scaffolds based on a melt-derived glass with the same composition was reported in order to investigate the effect of the synthesis route on the dissolution behavior and morphological features of the final biomaterials.

Keywords: Additive manufacturing; Bioactive glass; Sol-gel; Scaffolds; Bone tissue engineering.

1. Introduction

When dealing with health sciences, the reliability and reproducibility of manufacturing processes, as well as the need for achieving an accurate control on the characteristics of the final device, are considered not only technological goals but also moral imperatives to guarantee a safe and effective medical treatment to the patient [1].

Starting from the early 1980s, the introduction of solid freeform fabrication (SFF) technologies has been an important turning point in tissue engineering (TE), allowing an easy tailoring of scaffold properties by simply acting on process parameters [2], thus

minimizing, *inter alia*, operator-dependent tasks that could efficiently be replaced by dedicated instruction scrips and a properly-designed execution software [3], [4]. Robocasting is currently considered one of the most effective and powerful SFF methods for the processing of ceramics [5]–[8], glasses [9]–[12] and relevant composites [13], [14]. This technique is based on the continuous extrusion of a filament through a nozzle onto a building platform on which the 3D structure of the product is layer-wise built [15]. Application of robocasting to bioactive glasses (BGs) is not an easy task and is often associated to some critical issues due to the extreme reactivity of these biomaterials in aqueous environment [16]. For example, the use of 45S5 Bioglass® for ink production turned out to be quite challenging owing to the excessive leaching of Na^+ and the consequent increase in pH, which remarkably hindered an efficient dispersion of solid particles within the binder solution [17]. Despite these aspects, enthusiastic results were obtained by the processing of various BG compositions [9]–[12], opening up new possibilities in the use of strong 3D glass-based scaffolds in load-bearing applications.

In this regard, a great achievement related to the application of robocasting to BG-based materials was reported in 2014 by Eqtesadi et al. [18] who successfully produced vitreous grid-like 45S5 Bioglass® scaffolds with compressive strength (2-13 MPa) and total porosity (60-80 vol.%) suitable for BTE applications.

However, while robocasting of melt-derived glasses and their composites has been extensively experimented by several research groups, the processing of sol-gel–derived glasses by this technology is still poorly investigated. This paucity of studies has to be mainly attributed to the challenge of developing printable inks: in fact, mesoporous materials synthesized by the sol-gel process exhibit a highly different behavior upon

contact with liquids [19] as compared to non-porous glasses obtained by melt-quenching, which may cause additional issues in the ink preparation. In the case of glasses obtained by sol-gel chemical synthesis, most of the dispersing liquid in the ink is absorbed by the porous structure of the material, thus becoming unavailable for flowing. Ben-Arfa et al. [20], [21] recently managed this issue by optimizing simultaneously the heat treatment temperature, particle size, particle size distribution and porous fraction of the powder. These features, in fact, were found to be responsible of the packing ability and the flow behavior of the ink. In this way, scaffolds with different macropore sizes (300–500 μm) with solid loadings up to 40 vol.% were successfully obtained by robocasting technology starting from porous sol-gel glasses [20].

Another very common issue related to the processing of glass materials by robocasting deals with the poor stability of the amorphous network upon heating, which could induce devitrification within the system [22]–[25]. Using sol-gel glasses as basic materials within the ink composition may carry additional issues related to the effect of the high-temperature treatment on the meso-porosity, which could be significantly reduced and potentially determine a dramatical decrease in the bioactivity of the system. Furthermore, this inconvenient could likely compromise the entire functionality of highly-ordered mesoporous bioactive glasses (MBGs), whose synthesis is purposely designed to produce a nano-texture for hosting drugs and biomolecules [26].

In the past, the experimental 47.5B bioactive glass, a multicomponent silicate glass (47.5SiO_2-20CaO-10MgO-10Na_2O-10 K_2O-2.5P_2O_5, mol.%) produced by conventional melt-quenching route, was demonstrated to have a great potential as basic material for making printable inks with suitable features for robocasting technology in terms of printability and ink strength [10], [27], [28], as well as good thermal stability upon

sintering [29]–[31]. In this regard, Baino et al. [10] and Barberi et al. [27], [28] described the production of grid-like scaffolds characterized by uniform and gradient porosity with the aim of promoting fluid flow from the periphery to the core of the scaffolds while guaranteeing higher mechanical stability upon dissolution in physiological environment. In a recent study, Fiume and coworkers [32] reported for the first time the production and characterization of sol-gel materials based on the six-oxide 47.5B basic system aimed at selectively investigating the effect of the synthesis route on materials properties in terms of bioactivity, crystalline microstructure and texture as well as their variations depending on the calcination treatment. Despite calcination of sol-gel 47.5B-based material at 625 and 800°C led to devitrification, both sol-gel systems retained an excellent apatite-forming ability (i.e., bioactivity), which is key to obtain a good anchorage to the host tissue [32].

In the present work, for the first time we applied robocasting technology to 47.5B-based sol-gel multicomponent materials following a new and facile approach in which glass calcination treatments can be by-passed, thereby overcoming one of the most recurrent issues related to the design of sol-gel-based printable inks.

2. Materials and methods

2.1 Sol-gel synthesis

Multicomponent materials based on the silicate 47.5B compositional system 47.5SiO_2-2.5P_2O_5-20CaO-10MgO-10Na_2O-10K_2O (mol.%) were produced by sol-gel route, as described in a previous work [32].

The synthesis was carried out in acidic environment at room temperature under mild stirring conditions (200 rpm). Briefly, water and nitric acid were first mixed for 5 min

(H_2O: HNO_3 = 6, volumetric ratio); then, tetraethyl orthosilicate (TEOS) was added dropwise in a proper amount (H_2O : TEOS = 20, molar ratio). After 15 min, all the other reagents were sequentially added to the batch and the sol was mixed for 45 min more, until the complete dissolution of all the reagents was achieved. Specifically, triethyl phosphate (TEP), calcium nitrate tetrahydrate ($Ca(NO_3)_2 \cdot 4H_2O$), sodium nitrate ($NaNO_3$), magnesium nitrate hexahydrate ($(MgNO_3)_2 \cdot 6H_2O$) and potassium nitrate (KNO_3) were used as P_2O_5, CaO, Na_2O, MgO and K_2O sources, respectively.

Both gelation (room temperature, 72 h) and ageing (60 °C, 72 h) were carried out in sealed flasks to prevent the leak of organic compounds. Caps were then removed to perform drying (120 °C, 48 h) to allow the slow evaporation of the alcoholic liquid phase. The obtained dried gel, named DG-120, was then manually ground and sieved to get a final grain size between 38 and 150 μm and used as a basic material for the production of the DG-120 printable ink.

The parent melt-derived glass (MD-47.5B) was obtained by traditional melt-quenching in water as described elsewhere [29], [31], [32]. The obtained glass frit was milled (Pulverisette 0, Fritsch, Idar-Oberstein, Germany) and sieved (stainless steel sieve, Giuliani Tecnology Srl, turin, Italy) to get a final grain size below 32 μm and used as a basic material for the production of the MD-47.5B printable ink, used as reference.

2.2 Preparation of the printable inks and scaffold manufacturing

MD-47.5B and DG-120 were used as basic materials for the preparation of the printable inks for the robocasting system.

The ink formulation, optimized by means of some preliminary trials, included 65 vol.% of Pluronic F-127 solution and 35 vol.% of MD-47.5B and DG-120 particles for the reference and experimental ink, respectively. Pluronic F-127 was used consistently with

the experimental setup used in our previous works on the robocasting of melt-derived bioactive glass [10], [28].

The inks were prepared into small plastic pots so that only 2/3 of the total volume of the printing cartridge was filled, in order to efficiently manage the issues related to the stability of the ink over time.

The amounts of glass powder/dried gel and Pluronic F-127 solution were calculated knowing the density of each component according to Equation 1:

$$m_i = \frac{vol.\%_i \cdot V_f}{100} \cdot \frac{1}{\rho_i} \quad (1)$$

where m_i, $vol.\%_i$ and ρ_i are the mass, the volume percentage and the density of each component (ρ_{F127} = 1.067 g/cm^3, $\rho_{MD\text{-}47.5B}$ = 2.64 g/cm^3 [10], [28] and $\rho_{DG\text{-}120}$ =1.39 g/cm^3, assessed as mass-to-volume ratio), V_f is the final volume of melt-derived glass or dried gel considered to fill the cartridge up to 2/3 of its total volume (V_f = 3 and 6 ml for the MD-47.5B and the DG-120 ink, respectively).

The procedure followed for the production of MD-47.5B scaffolds was described in detail in a previous work [10], [28].

For the production of sol-gel–derived scaffolds, some modifications were introduced as compared to the original method described in Refs. [10], [28] on the basis of the different behavior of the materials upon mixing and extrusion. Briefly, DG-120 particles were suspended in the Pluronic-F127 solution under vigorous mixing (Vibrofix VF1 electronic, Ika-Werk; 2500 rpm, 1 min) until homogenization was achieved; then, the slurry was poured onto a clean substrate and hand-worked with a cold metal spatula until a moldable paste was obtained.

A Tabletop-3Dn printer (nScrypt Inc., Orlando, Florida, USA) with base set-up was used for robocasting. The pastes were transferred to the printing cartridge and extruded

under the following conditions: nozzle diameter 410 μm (Nordson EDF Optimum® SmoothFlow™), extrusion temperature within 20-24 °C, printing speed 2 mm/s and extrusion pressure within 0.83-1.10 bar and 1.24-1.45 bar for the DG-120 and MD-47.5B inks, respectively

Acetate sheets (Colour Copier and Laser Transparency OHP Film, Folex AG, Seewen, Switzerland) were used as printing substrates. Input parameters were inserted by means of a dedicated software (MachineTools3.0) provided by the manufacturer of the robocasting system.

After printing, the scaffolds were left to dry in an incubator at 37 °C for about 48 h in order to speed up the process and guarantee a more uniform drying over the whole volume, thus avoiding the formation of cracks. After drying, the greens were carefully detached from the acetate sheet and moved onto an alumina plate for sintering. Melt-derived and sol-gel scaffolds, named respectively RCS-md and RCS-sg, were obtained upon sintering treatment, setting a multistage heating program [32] and choosing a final temperature of 625 °C.

2.3. Scaffold characterization

Total porosity ε_0 of the scaffolds was assessed according to Equation 2 [33]:

$$\varepsilon_0 = 1 - \left({}^{\rho_s}/_{\rho_m}\right) \quad (2)$$

where ρ_s is the scaffold density (calculated as mass-to-volume ratio) and ρ_m is the density of the bulk material. Total porosity results were calculated on 10 samples for each type and expressed as mean value ± standard deviation.

The compressive strength of RCS-sg and RCS-md scaffolds was determined by crushing tests as L-to-A ratio, where L was the maximum load registered during the test and A was the initial cross-sectional area. Mechanical tests were performed by using an

MTS System Corp. apparatus with cross-head speed of 0.5 mm/min. Results are expressed as mean value ± standard deviation.

Scaffold bioactivity was investigated by immersion tests in Kokubo's simulated body fluid (SBF) [34] up to 14 days in mild-shaking conditions (100 rpm) to favor fluid circulation. A mass-to-volume ratio of 1.5 mg/ml was used, as suggested in a previous study by the Technical Committee 4 (TC04) of the International Commission on Glass (ICG) [35]. The variation of solution pH, resulting from the ion exchange between scaffold surface and fluid, was monitored at established time points, i.e. 6 h, 24 h, 48 h, 72 h, 168 h and 336 h. At the end of the experiments, samples were extracted from the solution, gently rinsed with distilled water and stored for further analyses.

Additionally, ion release from both scaffold types was investigated in vitro: at each time point, 1 ml of SBF was withdrawn and diluted with 9 ml of HNO_3 (1 M) to be analyzed by inductively coupled plasma optical emission spectroscopy (ICP-OES) (5110 ICP-OES, Agilent Technologies) in order to quantify the concentration of ions within the solution.

Morphological and compositional features of the scaffolds before and after immersion in SBF at different time points were investigated by field-emission scanning electron microscopy (SEM) coupled with energy-dispersive spectroscopy (EDS) (Supra TM 40, Zeiss, Oberkochen, Germany), using an inspection voltage of 15 kV. Before the analysis, scaffolds were sputter-coated with an ultrathin conductive layer of chromium (thickness ≈ 7 nm).

Moreover, microstructural surface modifications associated to the nucleation of calcium phosphates upon soaking were further investigated by X-ray diffraction analysis using a Bragg–Brentano camera geometry with a Cu Kα incident radiation (wavelength λ =

0.15405 nm). The 2θ angle varied within 10–70°, and the voltage and current were fixed at 40 kV and 30 mA, respectively. Data were collected with counting time of 1 s and step size of 0.02°. The analysis of crystalline phases was carried out by means of X'Pert HighScore software 2.2b (PANalytical, Eindhoven, The Netherlands), equipped with the PCPDFWIN database.

3. Results and discussion

Optical micrographs of as-printed melt-derived and sol-gel scaffolds before sintering are collected in Figure 1.

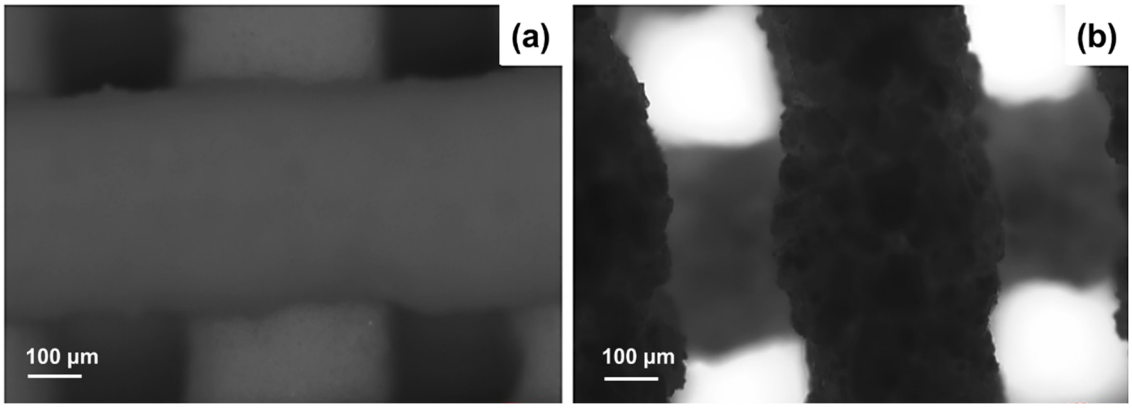

Figure 1. Optical images of robocast melt-derived and sol-gel materials based on the 47.5B composition: a) green bodies obtained using MD-47.5B ink and b) green bodies obtained by using DG-120 ink.

Both types of scaffolds exhibited a grid-like architecture made of parallel rectangular channels. Concerning the macroporous structure, there was no significant difference related to the use of different printing inks (i.e., melt-derived vs. sol-gel). Both images (Figures 1a and b), indeed, revealed high pattern regularity, although some bending was

observed close to the contact points between overlapped layers, determining some variations in the cross-sectional area of the rods.

The most striking distinction between the MD-47.5B and DG-120 inks was in the surface appearance, smooth and homogeneous in the first case (Figure 1a) and grainy in the latter (Figure 1b).

The geometrical/physical characteristics and derived parameters related to sintered scaffolds are collected in Table 1.

Table 1. Geometrical and physical characterization of grid-like RCS-md and RCS-sg scaffolds produced by robotic deposition of MD-47.5B- and DG-120-based inks, respectively (D_s, scaffold diameter; L_s, scaffold length; A_s, cross-sectional area; V_s, scaffold volume; m_s, scaffold mass; ε_0, scaffold porosity).

Scaffold type	**D_s/mm**	**L_s/mm**	**A_s/mm^2**	**V_s/mm^3**	**m_s/g**	**ε_0**
RCS-md	4.31±0.12	4.25±0.18	14.58±0.82	61.89±2.51	0.029±0.004	0.46±0.03
RCS-sg	4.24±0.15	4.17±0.11	14.14±1.01	58.98±4.84	0.089±0.004	0.81±0.03

As the printing code was the same for both scaffold types, primary geometrical features, i.e. scaffold height L_s and diameter D_s, were definitely comparable, with a minimum standard deviation calculated on 10 samples per each group. This is a further proof of the high reproducibility and reliability that could be obtained as a consequence of ink optimization.

On the contrary, the values of total porosity were significantly different between the two scaffold batches, being the porosity of sol-gel–derived scaffolds almost twofold as compared to melt-derived products.

In general, total porosity accounts both for open pores, i.e. macroscale pores deliberately created during the printing procedure, and for closed pores, typically associated to technological issues either related to the accidental closure of macro-pores or to suboptimal sintering conditions yielding residual interstitial porosity [30].

In both scaffold types, macro-porosity was constituted by parallel channels resulting from overlapped perpendicular rods. However, referring to Figure 2, some differences exist concerning the dimension of both rectangular pores and rods. In particular, the average thickness of the rods was considerably higher in *RCS-md* scaffolds compared to *RCS-sg* ones (340 μm vs. 260 μm). The cross-sectional area of the pores was consequently slightly larger in RCS-sg samples. This could be attributed to the higher shrinkage of the gel-based ink upon heating, which eventually led to thinner rods.

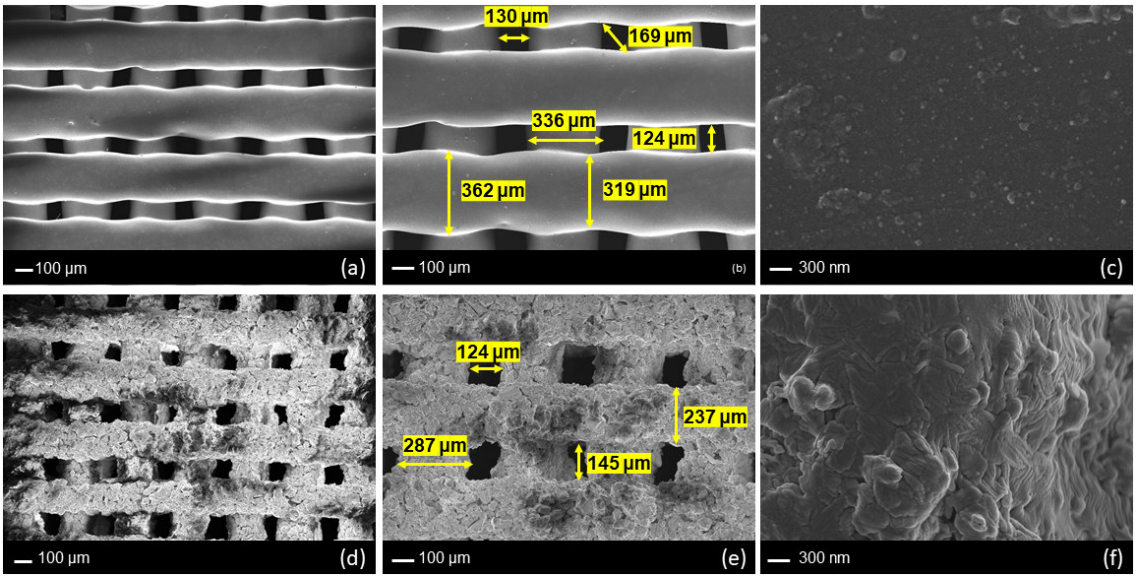

Figure 2. SEM images showing the morphology of grid-like sintered scaffolds obtained by robocasting technology: a), b), c) RCS-md and d), e), f) *RCS-sg* at different magnifications.

However, the doubling of total porosity in sol-gel–derived scaffolds cannot be attributed solely to the larger macro-pore size but inter-particles voids, which are clearly visible in Figure 2e, should be considered, too. Even upon thermal treatment, in fact, the surface of gel-derived scaffolds retained the same grainy appearance of green bodies (Figure 1b).

On the other hand, optimal densification levels were observed in *RCS-md* scaffolds sintered at 625 °C: in fact, unlike other 47.5B-derived scaffolds produced by conventional template-based manufacturing processes [30], [36], no inter-particle pores were visible after sintering and the scaffold surface appeared rather homogeneous and continuous (Figure 2c).

The choice of the thermal treatment was dictated by the need to ensure the slow and complete degradation of the binder upon heating: in this regard, the thermal

decomposition of Pluronic F127 is known to occur between 200 and 400 °C [37], well below the selected sintering temperature.

The compressive strength of RCS-sg scaffolds was assessed to be 5.0 ± 3.6 MPa, which is within the typical range reported for human cancellous bone (0.1-16 MPa) [38]. RCS-md scaffolds exhibited a fivefold higher compressive strength (25.0 ± 4.5 MPa); this significant difference can be attributed to the higher porosity of sol-gel materials (81 vs. 49 vol.%). Interestingly, the compressive strength of RCS-md scaffolds produced in this work is also fourfold higher than the strength obtained in a previous work on robocast cuboids fabricated by the same method and having an almost equal porosity (46 vs. 49 vol.%) [29]. This could be attributed to a scale effect related to the different sample size and shape (i.e. cylinder vs. cuboid, with the absence of sharp edges causing stress intensification in the former).

The stepwise evolution of *RCS-md* and *RCS-sg* surface upon soaking in SBF was characterized by means of XRD and SEM/EDS analyses, performed at different time points.

XRD patterns acquired on SBF-treated *RCS-md* (Figure 3a) and *RCS-sg* (Figure 3b) scaffolds for different time frames revealed the formation of hydroxyapatite (HA) on the surface of both sample types.

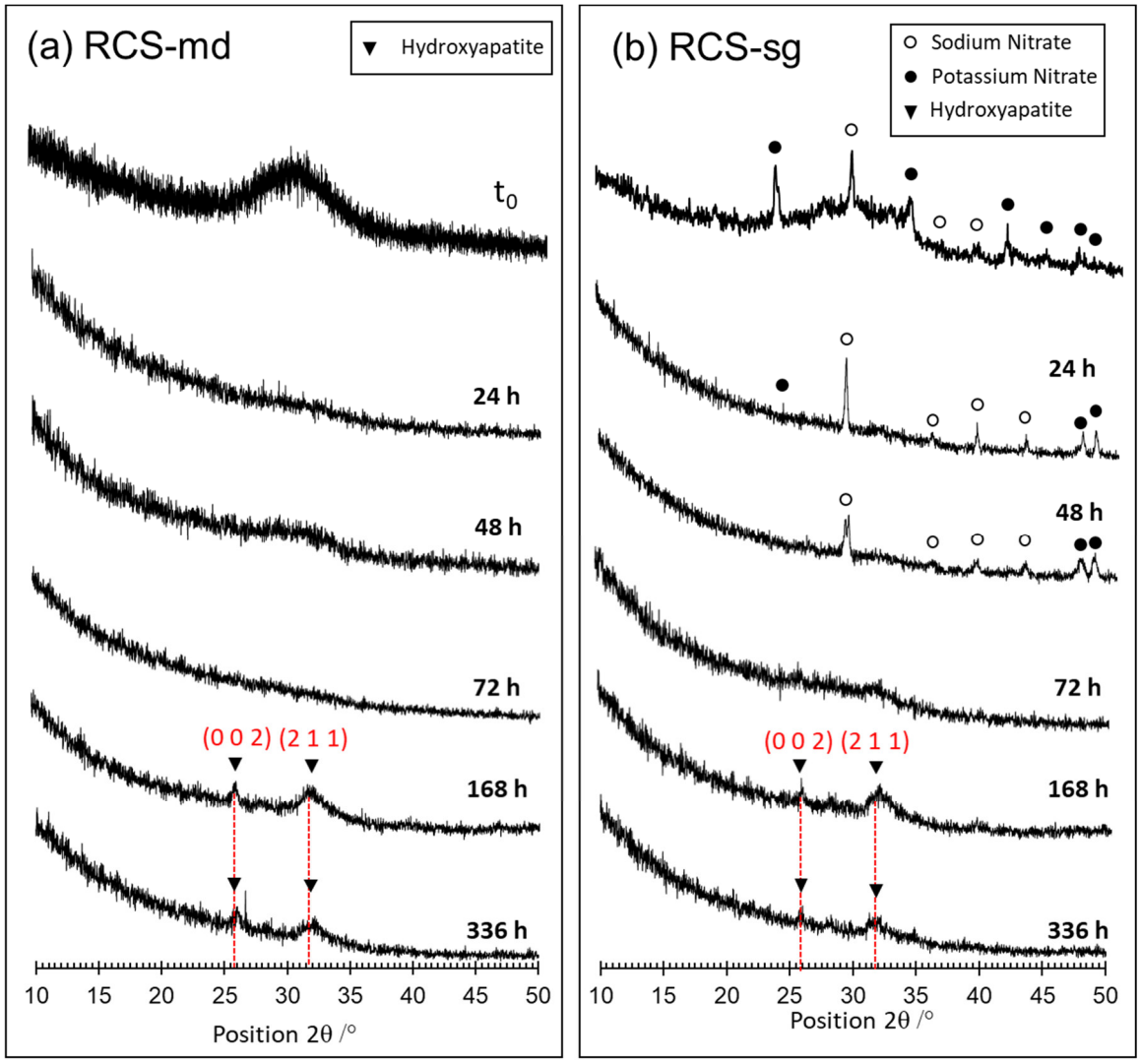

Figure 3. XRD analyses of *RCS-md* (a, left) and *RCS-sg* scaffolds (b, right) at different soaking times in SBF compared to un-soaked scaffolds (t_0). Characteristic peaks of HA are clearly visible after 1-week immersion in both sample sets, revealing a good HA-forming ability.

At $t = t_0$, the XRD pattern of *RCS-md* exhibited the typical amorphous halo of silica-based glassy materials. On the other hand, *RCS-sg* scaffolds displayed a basic amorphous halo along with multiple diffraction peaks related to the presence of residual nitrates within the sol-gel system up to 48 h-immersion ($NaNO_3$, ref. code: 01-072-0027 and KNO_3, ref. code: 01-073-1841), consistently with our previous results on the same

compositional system [32]. Other authors reported the thermal removal of calcium nitrate from sol-gel 45S5 compositional systems at around 530 °C [39], while sodium nitrate can be removed only at almost 800 °C [40]: this is consistent with the persistence of $NaNO_3$ in the XRD pattern of RCS-sg (Figure 3b).

After 3-day soaking, both the patterns revealed no well-defined diffraction peak, consistently with the progressive formation of a silica gel reaction layer, as expected in the typical bioactivity mechanism of bioactive glasses [41].

Although very weak diffraction signals were already visible at 72 h in RCS-sg, the two major characteristic peaks of HA were clearly appreciable after 1-week immersion at 25.7° (0 0 2) and 31.8° (2 1 1); the broadness of these peaks indicate the presence of a nano-crystalline structure [42].

SEM images related to RCS-sg are collected in Figure 4.

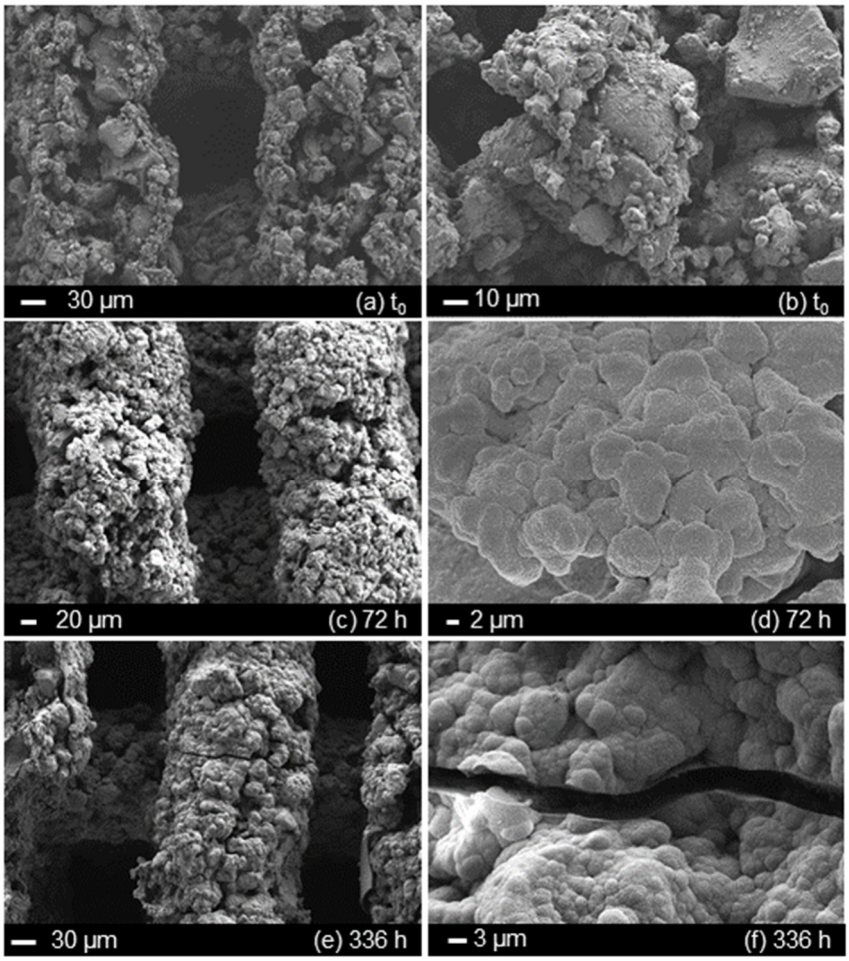

Figure 4. SEM micrographs showing the surface evolution upon soaking in SBF of *RCS-sg* at different time points: (a,b) scaffold before immersion, (c,d) after 72 h and (e,f) after 336 h (14 days).

Morphological surface assessments performed before and after immersion in SBF revealed an exceptional apatite-forming ability of the RCS-sg samples as a homogeneous layer of globular nanostructured HA was observed on the scaffold surface after just 72-h immersion; this is in good agreement with XRD results reported in Figure 3.

Figure 4f, acquired at higher magnification after 2-week immersion in SBF, clearly shows the “cauliflower arrangement” of HA globular agglomerates. The HA layer is

cracked because of the drying of the silica gel layer lying underneath and the high vacuum applied in the SEM chamber during morphological analyses.

Figure 5 shows the nanostructure of the HA layer formed on the surface of RCS-sg scaffold after 2-week immersion in SBF. The typical globular agglomerates of HA, resembling a cauliflower morphology, are characterized by characteristic needle-like nanocrystals; this is comparable to what previously observed by other authors [43].

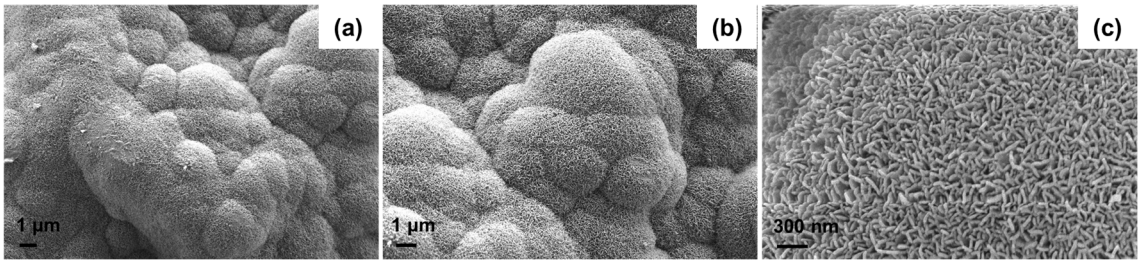

Figure 5. SEM micrographs at different magnifications (15.00 kX (a), 20.00 kX (b) and 100.00 kX (c)) showing the nanostructured morphology of HA formed on the surface of RCS-sg after immersion for 14 days in SBF.

In general, morphological results after immersion in SBF were found to be comparable with surface modifications observed by Baino et al. [10] and Barberi et al. [27], [28] for melt-derived 47.5B scaffolds produced by robocasting.

The pH variations within SBF, induced by ion-exchange mechanisms between the surface of the scaffold and the fluid, are displayed in Figure 6a.

The pH rapidly increased within the first 24 h post-immersion, as indicated by the sharp slope of the curve. Then, up to 3 days, the increase in pH slowed down. *RCS-sg* scaffolds induced a slightly higher pH increase over the first three days. However, after 72 h this trend reversed, leading to a higher increasing rate in *RCS-md* samples. Moreover, while the pH stabilized after 1-week immersion for sol-gel derived scaffolds,

a sustained increase up to 7.6 was observed for the melt-derived ones. This value was lower compared to that obtained in our previous study (~7.8) [10] because of the different sintering temperature (625 vs. 600 °C), yielding different densification, surface roughness and, hence, surface area available for ion exchange.

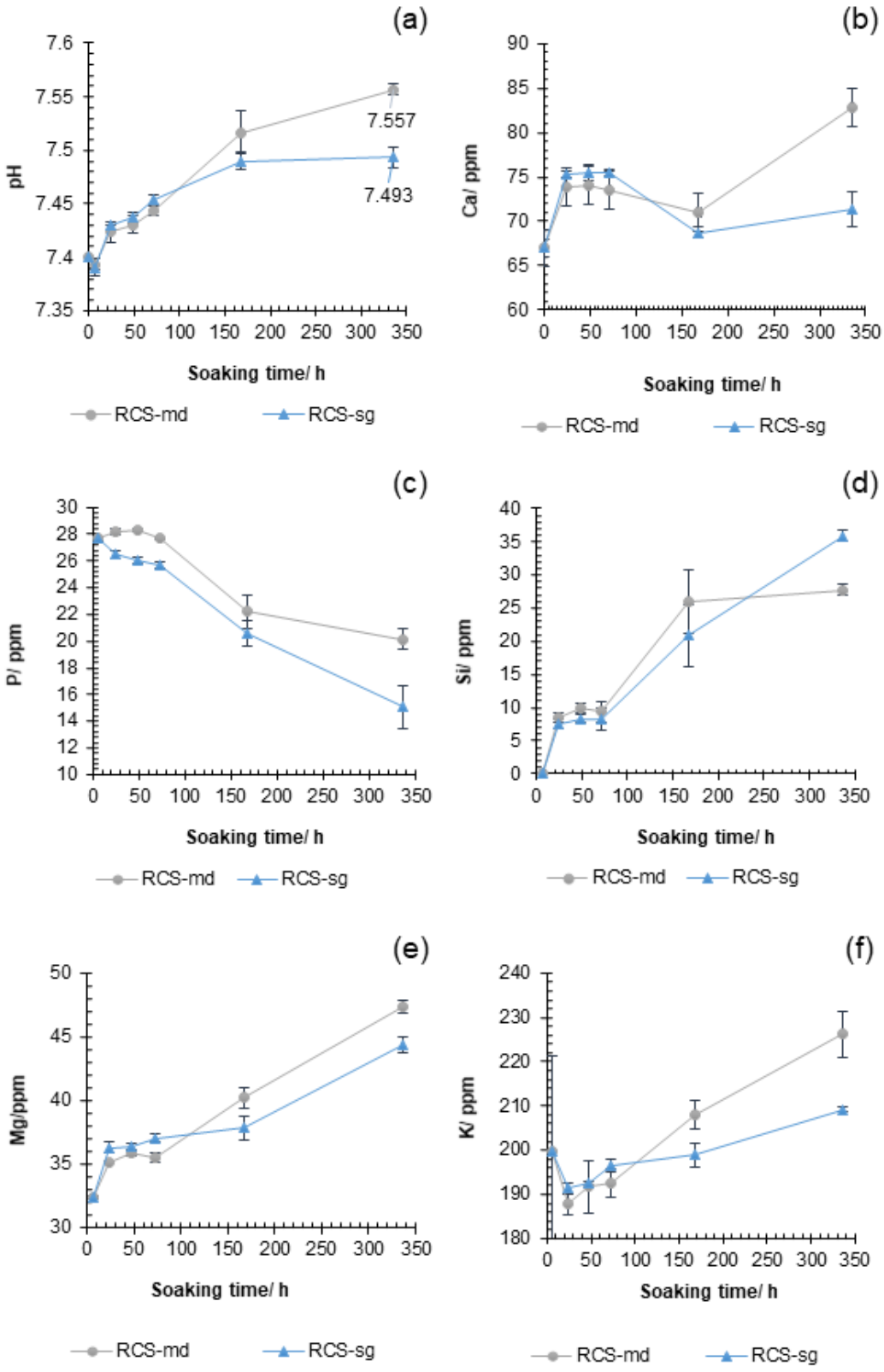

Figure 6. pH increase (a) and ion release profiles (b-f) upon soaking tests in SBF at different time points.

Unlike *RCS-md* scaffold, pH curve related to *RCS-sg* samples stabilized at pH~7.5 after just 1-week immersion. This result differs considerably from what previously seen for powdered samples, in which the pH increase related to 47.5B sol-gel powder was higher compared to melt-derived one, consistently with the higher SSA values obtained by BET analysis [32]. In this regard, it is possible that the interaction between 47.5B gel and F127-based binder solution led to some relevant modifications at molecular level, slowing down dissolution and ion release kinetics.

The release kinetics of Ca, P, Mg, Si and K were evaluated by ICP analysis, quantifying the concentration of these ions within the solution at different time points (Figure 6b-f). The release of sodium was not investigated: the high concentration of Na within the SBF composition, in fact, would result in the oversaturation of the detector used for the analysis, thus leading to unreliable results.

Even if comparable trends were observed for all the ionic species considered, regardless of the scaffold type considered, higher concentrations of ions within the solution were detected for the traditional melt-derived glass, in agreement with pH measurements reported in Figure 6a. In fact, according to the bioactivity mechanism commonly accepted for silica-based bioactive glasses [41], the pH of the physiologic solution is modified according to the extent of the ion exchange between the material and the fluid, gradually becoming less intense as the thickness of the HA surface layer increases upon soaking.

Calcium was rapidly released from both scaffold types within the first 24 h. Then, the concentration remained almost constant up to 72 h. On the other hand, phosphorus

reduction from SBF was observed, which is typically associated with the formation of a phosphate-rich layer on the glass surface, as also observed by other authors [44]. Actually, a sustained precipitation of calcium phosphate took place over the whole duration of the test. In fact, a significant decrease of both Ca and P was registered in the solution after 72-h immersion, corresponding to the formation of HA on the samples surface. This is in good agreement with SEM and XRD results previously discussed.

Mg, Si, and K trends were definitely consistent with the dissolution mechanism of silica-based bioactive glasses, exhibiting comparable trends characterized by a rapid increase within the first 24 h and an approximately constant part between 24- and 72-h soaking.

Concerning Si concentration, analogous trends were observed in the two systems up to 1 week, characterized by a sustained increase corresponding to the release of soluble $Si(OH)_4$ from the silica gel layer. However, while the curve related to melt-derived scaffolds (*RCS-md*) reached a plateau after 1 week, Si concentration for *RCS-sg* increased steadily until the end of the test. This result differs from previous studies on Si release from other sol-gel bioactive glasses, in which Si concentration tended to stabilize within 24 h from the beginning of the test [45-47]. It is reasonable to attribute this to a low polymerization of the silica network – perhaps due to the complexity of the multicomponent sol-gel system –, leading to more soluble silica available for dissolution. No relevant reports have been found in the current literature to support this hypothesis because of the paucity of comparative studies between melt-derived and sol-gel glasses with the same composition; this issue will deserve further investigation in future studies.

4. Conclusions

The present study describes, for the first time, the production of sol-gel–derived grid-like scaffolds by robocasting technology following a gel-based new, simplified strategy. Unlike other protocols reported in the literature, the ink formulation here developed did not require the use of any calcination treatment for producing "intermediate" glass particles to be incorporated in the ink, but the dried gel was directly used to prepare a printable paste. This is a double advantage that allows (i) reducing the time required for the overall process of scaffold fabrication and (ii) overcoming the risk of bioactivity decrease associated to multiple thermal treatments on sol-gel materials. Gel-based inks showed suitable extrusion behaviour for the robocasting processing, thus allowing the deposition of straight, parallel rods constituting the 3D architecture of the scaffolds. Gel-derived sintered scaffolds exhibited compressive strength comparable to that of human cancellous bone and good bioactive behaviour leading to the formation of calcium phosphates after just 72-h soaking in SBF, thus showing promise for application in bone tissue engineering. Given the chemical complexity of the system analysed (6-oxide 47.5B), it is believed that the development of robocasting inks based on gels with simpler compositions could be helpful in assessing the robustness of the overall procedure in more detail in future studies.

References

1. A. Bighamet al. The journey of multifunctional bone scaffolds fabricated from traditional toward modern techniques. Bio-Design Manuf. 3 (2020) 281–306.
2. M. Fazlollahi, Y. Pooshidani, M. Eskandari. Additive manufacturing in bone tissue engineering, in: S. Singh, C. Prakash, R. Singh (Eds.), 3D Printing in

Biomedical Engineering (Materials Horizons: From Nature to Nanomaterials), Springer, Singapore, 2020, pp. 95–125.
3. R. Gmeiner et al. Additive manufacturing of bioactive glasses and silicate bioceramics. J. Ceram. Sci. Tech. 06 (2015) 75-86.
4. O. Ivanova, C. Williams, T. Campbell. Additive manufacturing (AM) and nanotechnology: promises and challenges. Rapid Prototype J. 19 (2013) 353–364.
5. F. J. Martínez-Vázquez, F.H. Perera, P. Miranda, A. Pajares, F. Guiberteau. Improving the compressive strength of bioceramic robocast scaffolds by polymer infiltration. Acta Biomater. 6 (2010) 4361–4368.
6. P. Miranda, A. Pajares, E. Saiz, A.P. Tomsia, F. Guiberteau. Mechanical properties of calcium phosphate scaffolds fabricated by robocasting. J. Biomed. Mater. Res. - Part A 85 (2008) 218–227.
7. J. Franco, P. Hunger, M.E. Launey, A.P. Tomsia, E. Saiz. Direct write assembly of calcium phosphate scaffolds using a water-based hydrogel. Acta Biomater. 6 (2010) 218–228.
8. J.A. Lewis, J.E. Smay, J. Stuecker, J. Cesarano. Direct ink writing of three-dimensional ceramic structures, J. Am. Ceram. Soc. J. Am. Ceram. Soc. 89 (2006) 3599–3609.
9. S. Eqtesadi, A. Motealleh, A. Pajares, F. Guiberteau, P. Miranda. Improving mechanical properties of 13 – 93 bioactive glass robocast scaffold by poly (lactic acid) and poly (ε -caprolactone) melt in fi ltration. J. Non. Cryst. Solids 432 (2016) 111–119.
10. F. Baino et al. Robocasting of Bioactive SiO2-P2O5-CaO-MgO-Na2O-K2O Glass Scaffolds. J. Healthc. Eng. 2019 (2019) 5153136.
11. S. Eqtesadi et al. Robocasting of 45S5 bioactive glass scaffolds for bone tissue engineering. J. Eur. Ceram. Soc. 34 (2014) 107–118.+
12. A.M. Deliormanli, M.N. Rahaman. Direct-write assembly of silicate and borate bioactive glass scaffolds for bone repair. J. Eur. Ceram. Soc. 32 (2012) 3637–3646.
13. J. Cesarano. Robocasting of ceramics and composites using fine particle suspensions. University Libraries UNT Digital Library (1999).
14. A. Motealleh, S. Eqtesadi, A. Civantos, A. Pajares, P. Miranda. Robocast 45S5 bioglass scaffolds: in vitro behavior. J. Mater. Sci. 52 (2017) 9179–9191.
15. E. Fiume, F. Baino. Robocasting of mesoporous bioactive glasses (MBGs) for bone tissue engineering, in: A. Osaka, R. Narayan (Eds.) Bioceramics-From Macro to Nanoscale, Elsevier, 2020, pp. 327–349.
16. R.S. Pryce, L.L. Hench. Dissolution Characteristics of Bioactive Glasses. KEM 240–242 (2003) 201–204.
17. B.A.E. Ben-Arfa et al. Robocasting of ceramic glass scaffolds: Sol–gel glass, new horizons. J. Eur. Ceram. Soc. 39 (2019) 1625–1634.
18. S. Eqtesadi et al. Robocasting of 45S5 bioactive glass scaffolds for bone tissue engineering. J. Eur. Ceram. Soc. 34 (2014) 107–118.
19. D. Arcos, M. Vallet-Regí. Sol-gel silica-based biomaterials and bone tissue regeneration. Acta Biomater. 6 (2010) 2874–2888.

20. B.A.E. Ben-Arfa, R.C. Pullar. A comparison of bioactive glass scaffolds fabricated by robocasting from powders made by sol-gel and melt-quenching methods. Processes 8 (2020) 615.
21. B.A.E. Ben-Arfa, I.M. Miranda Salvado, J.M.F. Ferreira, R.C. Pullar. A hundred times faster: Novel, rapid sol-gel synthesis of bio-glass nanopowders (Si-Na-Ca-P system, Ca:P = 1.67) without aging. Int. J. Appl. Glas. Sci. 8 (2017) 337–343.
22. M.O. Prado, E.B. Ferreira, E.D. Zanotto. Sintering kinetics of crystallizing glass particles. a review. Ceram. Trans. 170 (2005) 163–179.
23. W. Holand, G.H. Beall. Glass Ceramic Technology, John Wiley & Sons, 2019.
24. C. Blaeß, D.S. Brauer. Sintering and concomitant crystallization of bioactive glasses. Int. J. Appl. Glass Sci. 10 (2019) 449–462, doi:10.1111/ijag.13477.
25. J. Malek. Kinetic analysis of crystallization processes in amorphous materials. Thermochim. Acta 355 (2000) 239–253.
26. G.J. Owens et al. Sol-gel based materials for biomedical applications. Prog. Mater. Sci. 77 (2016) 1–79.
27. J. Barberi et al. Mechanical characterization of pore-graded bioactive glass scaffolds produced by robocasting. Biomed. Glas. 5 (2019) 140–147.
28. J. Barberi et al. Robocasting of SiO2-based bioactive glass scaffolds with porosity gradient for bone regeneration and potential load-bearing applications. Materials 12 (2019) 2691.
29. E. Fiume, E. Verné, F. Baino. Crystallization behavior of SiO2–P2O5–CaO–MgO–Na2O–K2O bioactive glass powder. Biomed. Glas. 5 (2019) 46–52.
30. E. Fiume et al. Comprehensive assessment of bioactive glass and glass-ceramic scaffold permeability: experimental measurements by pressure wave drop, modelling and computed tomography-based analysis. Acta Biomater. 119 (2020), 405-418.
31. E. Fiume, G. Serino, C. Bignardi, E. Verné, F. Baino. Sintering Behavior of a Six-Oxide Silicate Bioactive Glass for Scaffold Manufacturing. Appl. Sci. 10 (2020) 8279.
32. E. Fiume, C. Migneco, E. Verné, F. Baino. Comparison between Bioactive Sol-Gel and Melt-Derived Glasses/Glass-Ceramics Based on the Multicomponent SiO2–P2O5–CaO–MgO–Na2O–K2O System. Materials 13 (2020) 540.
33. V. Karageorgiou, D. Kaplan. Porosity of 3D biomaterial scaffolds and osteogenesis. Biomaterials 26 (2005) 5474–5491.
34. T. Kokubo, H. Takadama. How useful is SBF in predicting in vivo bone bioactivity? Biomaterials 27 (2006) 2907–2915.
35. A.L.B. Macon et al. A unified in vitro evaluation for apatite-forming ability of bioactive glasses and their variants. J. Mater. Sci. Mater. Med. 26 (2015) 115.
36. E. Fiume, G. Serino, C. Bignardi, E. Verné, F. Baino. Bread-derived bioactive porous scaffolds: an innovative and sustainable approach to bone tissue engineering. Molecules 24 (2019) 2954.
37. Q. Dou, A.A. Karim, X.J. Loh. Modification of thermal and mechanical properties of PEG-PPG-PEG copolymer (F127) with MA-POSS. Polymers (Basel) 8 (2016) 341.

38. L.-C. Gerhardt, A.R. Boccaccini. Bioactive Glass and Glass-Ceramic Scaffolds for Bone Tissue Engineering. Materials (Basel) 3 (2010) 3867–3910.
39. I. Cacciotti, M. Lombardi, A. Bianco, A. Ravaglioli, and L. Montanaro. Sol-gel derived 45S5 bioglass: Synthesis, microstructural evolution and thermal behaviour. Journal of Materials Scince: Materials in Medicine 23 (2012) 1849–1866.
40. K. Zheng *et al.* Aging time and temperature effects on the structure and bioactivity of gel-derived 45S5 glass-ceramics. Journal of the American ceramic Society 98 (2015) 30-38.
41. D.-C. Greenspan. Bioactive glass: mechanisms of bone bonding. Tandläkartidningen Årk 91 (1999) 1–32.
42. D.A.N.N. Ungureanu, N. Angelescu, R.M. Ion, E.V. Stoian, C.Z. Rizescu. Synthesis and Characterization of Hydroxyapatite Nanopowders by Chemical Precipitation. Proceeding of 10th WSEAS international conference on electronics, hardware, wireless and optical communications, and 10th WSEAS international conference on signal processing, robotics and automation, and 3rd WSEAS international conference on nanotechnology, and 2nd WSEAS international conference on Plasma-fusion-nuclear physic (2011) 296–301.
43. D. Ksouri et al. Synthesis of ternary bioactive glass derived aerogel and xerogel: study of their structure and bioactivity. Nova Biotechnologica et Chimica 17 (2018) 150-159.
44. A. Nommeots-Nomm et al. Highly degradable porous melt-derived bioactive glass foam scaffolds for bone regeneration. Acta Biomaterialia 57 (2017) 449–461.
45. Q.-Z. Chen, G.A. Thouas. Fabrication and characterization of sol–gel derived 45S5 Bioglass®–ceramic scaffolds, Acta Biomaterialia 7 (2011) 3616-3626.
46. P. Sepulveda, J. R. Jones, L. L. Hench. *In vitro* dissolution of melt-derived 45S5 and sol-gel derived 58S bioactive glasses. Journal of Biomedical Materials Research (2002) 301-311.
47. D. Arcos, D. C. Greenspan, M. Vallet-Regı´. Influence of the Stabilization Temperature on Textural and Structural Features and Ion Release in SiO2-CaO-P2O5 Sol-Gel Glasses, Chemistry of Materials 14 (2002), 1515-1522.